

מכון ויצמן למדע

WEIZMANN INSTITUTE OF SCIENCE



Surface-Guided CsPbBr₃ Perovskite Nanowires on Flat and Faceted Sapphire with Size-Dependent Photoluminescence and Fast Photoconductive Response

Document Version:

Accepted author manuscript (peer-reviewed)

Citation for published version:

Oksenberg, E, Sanders, E, Popovitz-Biro, R, Houben, L & Joselevich, E 2018, 'Surface-Guided CsPbBr₃ Perovskite Nanowires on Flat and Faceted Sapphire with Size-Dependent Photoluminescence and Fast Photoconductive Response', *Nano Letters*, vol. 18, no. 1, pp. 424-433.
<https://doi.org/10.1021/acs.nanolett.7b04310>

Total number of authors:

5

Digital Object Identifier (DOI):

[10.1021/acs.nanolett.7b04310](https://doi.org/10.1021/acs.nanolett.7b04310)

Published In:

Nano Letters

General rights

@ 2020 This manuscript version is made available under the above license via The Weizmann Institute of Science Open Access Collection is retained by the author(s) and / or other copyright owners and it is a condition of accessing these publications that users recognize and abide by the legal requirements associated with these rights.

How does open access to this work benefit you?

Let us know @ library@weizmann.ac.il

Take down policy

The Weizmann Institute of Science has made every reasonable effort to ensure that Weizmann Institute of Science content complies with copyright restrictions. If you believe that the public display of this file breaches copyright please contact library@weizmann.ac.il providing details, and we will remove access to the work immediately and investigate your claim.

Surface-Guided CsPbBr₃ Perovskite Nanowires on Flat and Faceted Sapphire with Size-Dependent Photoluminescence and Fast Photoconductive Response

Eitan Oksenberg[†], Ella Sanders[†], Ronit Popovitz-Biro[‡], Lothar Houben[‡] and Ernesto Joselevich^{†}*

[†]Department of Materials and Interfaces and [‡]Chemical Research Support, Weizmann Institute of Science, Rehovot, 76100, Israel.

KEYWORDS: photodetector, planar, epitaxy, photoresponse, halide perovskite.

ABSTRACT

All-inorganic lead halide perovskite nanowires have been the focus of increasing interest since they exhibit improved stability compared to their hybrid organic-inorganic counterparts, while retaining their interesting optical and optoelectronic properties. Arrays of surface-guided nanowires with controlled orientations and morphology are promising as building blocks for various applications and for systematic research. We report the horizontal and aligned growth of CsPbBr₃ nanowires with a uniform crystallographic orientation on flat and faceted sapphire surfaces to form arrays with 6-fold and 2-fold symmetries, respectively, along specific directions

of the sapphire substrate. We observed waveguiding behavior and diameter-dependent photoluminescence emission well beyond the quantum confinement regime. The arrays were easily integrated into multiple devices, displaying p-type behavior and photoconductivity. Photodetectors based on those nanowires exhibit the fastest rise and decay times for any CsPbBr₃-based photodetectors reported so far. One-dimensional arrays of halide perovskite nanowires are a promising platform for investigating the intriguing properties and potential applications of these unique materials.

TEXT

Lead halide perovskites have re-emerged as highly interesting optoelectronic materials.¹ They generate enormous interest mostly for low temperature, low-cost solar cells,^{2, 3} but also for other optoelectronic applications including photodetectors, LEDs and laser devices.⁴⁻⁶ Their unique optoelectronic properties have been attributed to long electronic carrier diffusion lengths, photon recycling, high optical absorption coefficients and low trap density.⁷⁻¹⁰ However, despite extensive investigation, various observed phenomena and some of their fundamental properties are still not fully understood, especially hysteresis phenomena and disorder in their crystal structure.¹⁰⁻¹³ Nanowires (NWs) of lead halide perovskites have exhibited some interesting properties as well, including low threshold lasing at room temperature⁴ and polarity-dependent photodetection.⁶ Besides their potential use as building blocks for various applications, their one-dimensional nature can facilitate the investigation and modeling of some phenomena that are not yet well understood including photon and charge carrier transport.

Recently, due to stability issues, some focus has shifted from hybrid organic-inorganic perovskites to the more robust and stable all inorganic perovskites.¹⁴ Cs-based lead halide

perovskite were found to be both stable and promising for solar cell applications,^{15, 16} and CsPbX₃ (X=Cl,Br,I) NWs proved to be a versatile system as their composition and corresponding emission is easily tunable through anion exchange. In addition, they are stable in air and can act as high-quality laser cavities.¹⁷⁻¹⁹ As in the case of more traditional semiconductor NWs, planar and aligned arrays of CsPbX₃ NWs with controlled morphology and crystallographic orientation can be highly advantageous for both applications and research. However, unlike more traditional semiconductor surface-guided NWs, CsPbBr₃ NWs do not grow by the common nanoparticle-catalyzed vapor-liquid-solid (VLS) growth mechanism but by a non-catalyzed direct vapor-solid (VS) growth. This non-catalyzed growth can present new challenges when pursuing surface-guided NWs because the mechanism of nucleation and elongation that determine the location and one-dimensionality in the VLS process, respectively, are not known for such a VS process. Lately two groups demonstrated Van-der-Waals incommensurately epitaxial growth of CsPbX₃ microwires and NWs in six directions on mica substrates.^{20, 21} Growth in six directions leads to random triangular-shaped networks, which are less useful for integration into devices than parallel arrays (i.e. one or two opposite growth directions). Graphoepitaxy on faceted substrates has been shown to guide the growth of parallel arrays of various semiconductor NWs and enable their integration into devices.²²⁻²⁹ Applying this principle to produce parallel arrays of halide perovskite NWs would similarly enable their integration into devices. Moreover, a comparative investigation of epitaxial and graphoepitaxial growth of CsPbX₃ NWs, their crystal structure and properties on different substrates was not yet conducted.

Here we employ a guided growth approach that uses epitaxial and graphoepitaxial relationships between the material and substrate to guide horizontal CsPbBr₃ NWs during their growth to create well aligned arrays of NWs that grow in specific and reproducible directions and crystallographic

orientations. We demonstrate graphoepitaxial growth of CsPbBr₃ that results in an advantageous bidirectional growth (figure 1A) as horizontal and aligned NWs grow along nanogrooves on a faceted sapphire plane. We also show epitaxial growth on a flat sapphire substrate where horizontal and aligned NWs grow along six isoperiodic directions of the flat sapphire plane (figure 1B). We characterized the crystal structure, crystallographic orientation and elemental composition of the CsPbBr₃ NWs by cutting thin lamellae across and along the growth axis of the NWs and examining them under a high resolution transmission electron microscope (HRTEM). We find that all the NWs have a triangular cross-section and that they grow along the same [001] crystallographic orientation of the CsPbBr₃ cubic phase. Optical characterization of NWs with varying diameters revealed waveguiding behavior and diameter-dependent photoluminescence (PL) well beyond the quantum confinement regime. In order to probe the electronic and optoelectronic properties of CsPbBr₃ guided NWs, we exploited the ordered arrays of NWs and integrated them into multiple devices in a parallel and simple manner. We demonstrated field-effect transistors (FETs) and photodetectors based on an array of few CsPbBr₃ guided NWs. The photodetectors exhibit the fastest response times for any CsPbBr₃ based photodetector reported so far.^{21, 30-38}

The vapor-phase growth of the guided CsPbBr₃ NWs was carried out in a three-zone tube furnace (see Supporting Information for details). The NWs grow non-catalyzed almost exclusively horizontally and aligned on bare, faceted, annealed M-plane sapphire substrate (figure 1A) and on flat C-plane sapphire (figure 1B). All the NWs have a triangular cross-section with heights ranging from 20 nm to a few microns. Careful attention to growth conditions and the duration of the process can afford NWs with different dimensions. However, some variation was evident in all our growth attempts. The growth conditions control also the density of the NWs, as well as the density of other structures, such as rectangular platelets and triangular pyramids, that can also form in similar

growth conditions. The typical length of the NWs is few tens of microns, although extremely long wires (hundreds of microns) were also observed under certain growth conditions.

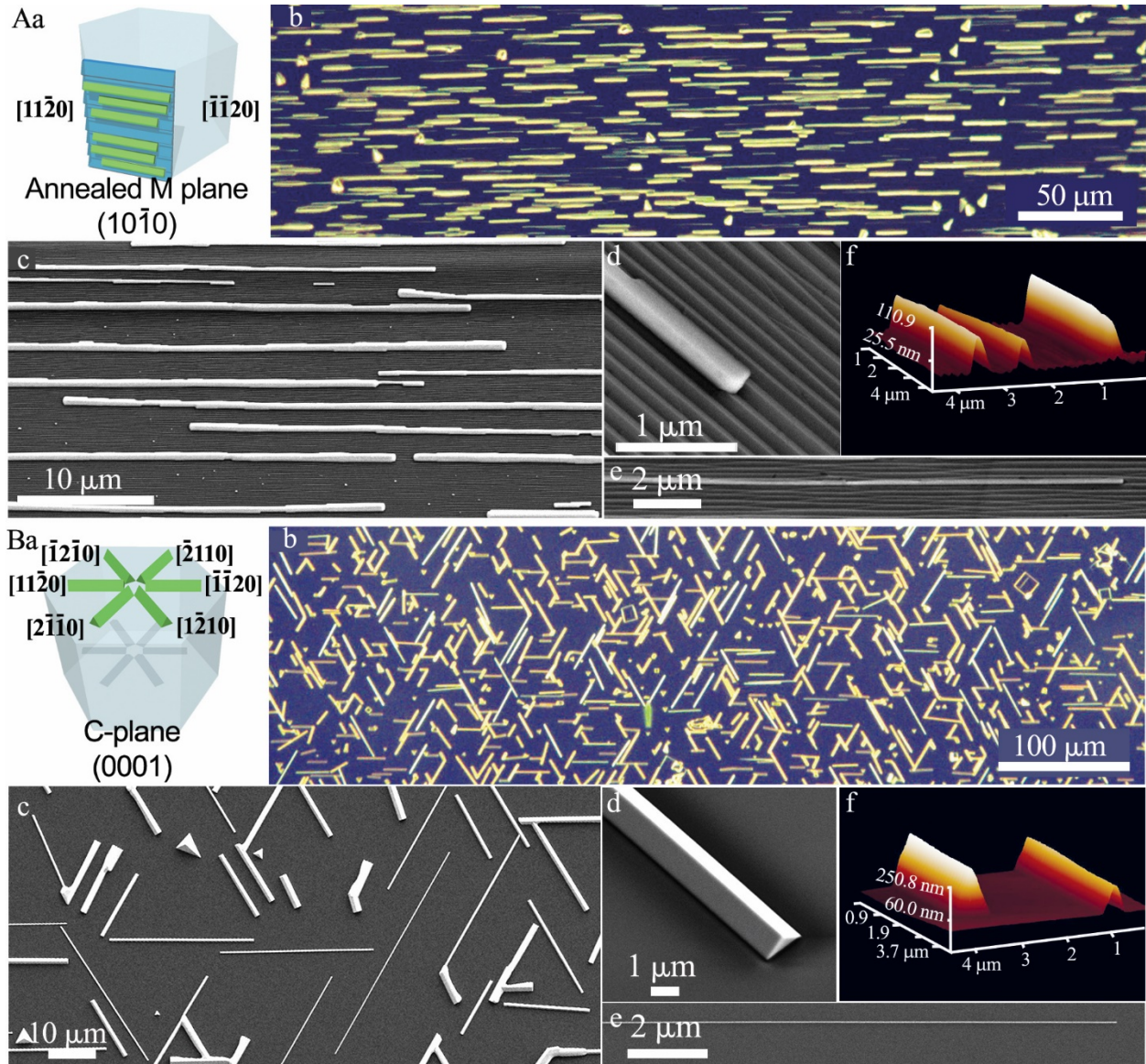


Figure 1. Guided growth of (A) graphoepitaxial and (B) epitaxial CsPbBr₃ nanowires. For each growth mode: (a) A schematic illustration of the plane and directional growth. (b) A dark-field optical microscope image of a typical growth. SEM images of (c) an assembly of NWs and higher

magnification images of (d) a thick and (e) a thin NW. (f) 3D AFM image revealing the triangular cross-section of the NWs.

On flat C (0001) sapphire, the guided CsPbBr₃ NWs grow along the six isoperiodic $A \pm \langle 11\bar{2}0 \rangle$ directions, reflecting the symmetry of the substrate. The six-directional growth behavior resembles previous guided growth reports of GaN,²⁷ ZnO,²⁶ ZnSe,²³ ZnTe²⁴, CdSe²⁵, core-shell ZnSe@ZnTe²² and CdS²⁸ NWs on C-plan sapphire. However, while in all those previous reports the NWs grow along six $M \pm \langle 10\bar{1}0 \rangle$ directions, here the CsPbBr₃ NWs grow along six $A \pm \langle 11\bar{2}0 \rangle$ directions of the sapphire substrate. HRTEM imaging of lamellae cut across the NWs using a focused ion beam microscope (FIB) unveil the distinct isosceles right triangle cross-section structure. Selected area fast Fourier transform (FFT) of these cross-sections, along with additional crystallographic information retrieved from lamellae that were cut along the growth axis of the NWs, allow us to determine their crystallographic structure: All 7 CsPbBr₃ NWs that were analyzed have a cubic crystal structure. They grow as triangular prisms with a [001] growth axis as their (110) planes are parallel to the (0001) planes of the sapphire, and the (100) and (010) facets are exposed to the gas phase (figure 2B-C and figure S2). In addition to these TEM analyses, we performed powder XRD measurements of the as grown CsPbBr₃ NWs on the C-plane sapphire. The diffractogram (figure S3) shows that both orthorhombic and cubic phases coexist in our sample. The cubic phase is consistent with our TEM analyzes, which show that all the surface-guided NWs are cubic, while the orthorhombic phase could arise from bulkier by-products, such as pyramids, platelets and less defined deposits, which may adopt the crystal structure that is more stable in the bulk.

The growth directions and the crystallographic orientation of the NWs are very consistent. Examining their cross-section reveals that, as expected for epitaxial growth, the transverse ($\bar{1}10$)

planes (planes that are orthogonal to the substrate and to the axis of the NW) are aligned with the ($\bar{1}100$) of the sapphire (figure 2B(d)). These planes were suggested as the dominant factor at determining the crystallographic orientation for guided NWs in high-mismatch systems.³⁹ However, we must acknowledge that with CsPbBr₃ NWs some of the known guidelines of horizontal growth may not be relevant. Besides the very different structure of this material, the growth mechanism of these CsPbBr₃ NWs is inherently different from the more traditional vapor-liquid-solid (VLS) guided horizontal growth. In this case, there is no catalyst and thus the planes do not form at the liquid-solid interface. For further crystallographic characterization we also examined the long dimension of a NW through a lamella that was cut along the axis of a NW. Again the epitaxial alignment of the sapphire and CsPbBr₃ lattices are evident (figure 2B(g)).

One of the strengths of the guided growth approach is the ability to control the growth direction of the horizontal NWs through surface manipulation. Past studies have shown that NWs can grow along nanosteps and nanogrooves on nanofaceted sapphire substrate, and that this growth mode, which we refer to as graphoepitaxy, has proven to be dominant over the epitaxial growth of the NWs.²²⁻²⁷ In order to explore the graphoepitaxial growth of CsPbBr₃ NWs we create a faceted substrate by annealing the thermodynamically unstable flat M ($10\bar{1}0$) sapphire at elevated temperatures (i.e. 1600°C). This creates an accordion-like surface of periodic nanogrooves with alternate S-plane and R-plane facets.⁴⁰

As seen in figure 2A, the horizontal CsPbBr₃ NWs grow along the two $\pm\langle 11\bar{2}0 \rangle$ directions of the sapphire nanogrooves. HRTEM imaging of lamellae cut across the NWs expose again a triangular cross-section. Furthermore, selected area FFT of these cross-sections reveal that all 17 NWs that were analyzed have the same cubic crystal structure and crystallographic orientation as the NWs that grow on the flat C- plane substrate. Despite the drastically different morphology and

structure of the two substrates, on both substrates the CsPbBr₃ consistently grow as triangular prisms with the same [001] growth axis and with the (100) and (010) facets that form the exposed sides of the prism (figure 2C).

When comparing the growth results of the CsPbBr₃ horizontal NWs to previous studies on horizontally aligned NWs that grow in a VLS mechanism,²²⁻²⁷ some differences are evident. In most cases of guided VLS growth, the graphoepitaxially guided NWs had a high degree of non-uniformity in their crystallographic orientation and rougher surfaces compared to NWs that grew on flat surfaces.²²⁻²⁵ We hypothesized that strain accumulates in the graphoepitaxial NWs since they have to adapt simultaneously to two different sapphire planes and their energetic constraints, which is manifested in a rougher surface and lesser uniformity in their growth axes.²³ In contrast, all the CsPbBr₃ horizontal NWs that grow on the nanogrooved substrate have the exact same crystallographic orientation and their surfaces appear to be as smooth as the guided NWs that grow on the flat substrate. These differences imply that the perovskite guided NWs can accommodate more easily to very different substrate morphologies and adapt to strenuous conditions without changing their own crystal structure. This might be a result of the dynamic nature of lead halide perovskites.¹² Another phenomenon that can be attributed to the same type of dynamic behavior is the ability of the guided NWs that grow along the nanogrooves to change their width by changing the number of grooves they grow on without an apparent effect on their surface morphology or crystallographic orientation (figure S4).

We note that for almost all of the NWs that were analyzed, both epitaxial and graphoepitaxial, we found peaks in the selected area FFT that correspond to lattice distances that match half a unit cell (Figure S5). Currently we cannot attribute these peaks with certainty to a single phenomenon. We can however state that the origin of the half unit cell peaks is most likely either phase domain

boundaries or Ruddlesden–Popper domains within the CsPbBr₃ NWs. Both phenomena are well known for oxide perovskites, and both were observed at least once in CsPbBr₃ structures.^{41, 42} In order to determine which structural phenomenon is present in our CsPbBr₃ NWs, atomic level aberration-corrected scanning TEM (STEM) analysis is needed.⁴³ We intend to pursue this route in order to understand the crucial role of the structure in determining the properties of these NWs.

It should be noted that CsPbBr₃ is beam-sensitive and undergoes different compositional and formational changes under high beam doses.⁴⁴ For the HRTEM imaging we used high spot sizes that correspond to low doses of irradiation, However to perform a non-destructive compositional analysis we preferred to use STEM EDS measurements on a FEI Tecnai F-20 microscope with 120 keV acceleration voltage and 1nA beam current. 90 EDS spectra were taken from an area of about 70 nm² in the center of the NW (figure 2B(e)). The spectra were summed in order to improve the signal to noise ratio and to achieve a quality quantification. The composition quantification was done using the L lines of the elements and an elemental ratio of 1:1.2:3.2 for the Cs, Pb and Br respectively was determined, in close agreement and within the range of error for the CsPbBr₃ phase.

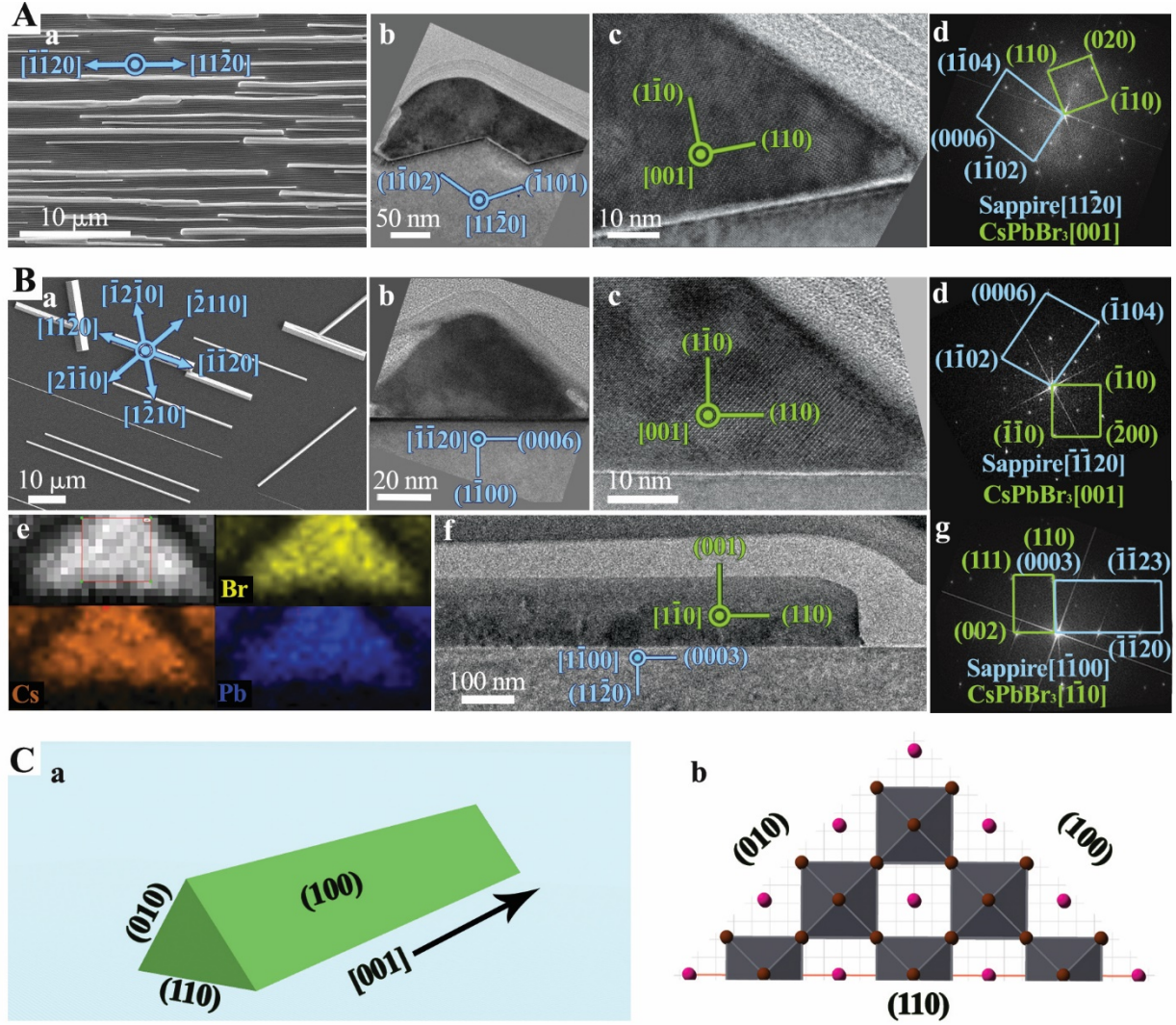


Figure 2. Crystallographic analysis of CsPbBr₃ NWs on Annealed M-plane (A) and C-plane (B) sapphire. For each plane: (a) SEM image of the guided nanowires, the blue indices and vectors describe the sapphire crystallographic directions. (b) HRTEM cross-section image marked with the crystal planes and direction of the sapphire substrate (blue). (c) Higher magnification image marked with the crystal planes and direction of the CsPbBr₃ NW (green). (d) Selected area fast Fourier transform (FFT) of the cross-section image. For C-plane sapphire added images of (e) STEM EDS elemental maps for Br, Cs and Pb together with the corresponding high angle annular dark field (HAADF) map. The red rectangle in the HAADF map is the area from which the EDS

spectra were taken for quantitative analysis. (f) HRTEM cross-section image marked with the crystal planes and direction of the sapphire substrate (blue) and the CsPbBr₃ nanowire (green). (g) Selected area fast Fourier transform (FFT) of the cross-section image. (C) Illustration of the morphology of the CsPbBr₃ guided NWs (a) and their crystal structure (b).

Unlike previous cases where guided NWs form in a VLS mechanism, the guided CsPbBr₃ NWs are not catalyzed. Therefore it is reasonable to expect different and perhaps new growth behaviors. For instance, we did not observe any order in the nucleation sites. The nucleation of these nanostructures appears to be random, or in some cases, mildly affected by defects or impurities of the substrate. The exact mechanism of the nucleation and growth of these NWs is not clear, nor is their relationship with the substrate and how it affects their growth direction and crystallographic orientation. Nonetheless, we can combine several empirical observations and postulate guidelines that reflect our understanding of the process.

The first and perhaps most important observation is the uniformity of the crystallographic orientation in almost all reported vapor-phase growth of CsPbBr₃ NWs. In almost all the reports the CsPbBr₃ NWs have the same [001] growth axis and the same cubic crystal structure.^{20, 21, 45} The only exception is one report of a monoclinic phase.⁴⁶ Moreover, in all cases of surface-bound growth, either incommensurate Van-der-Waals epitaxy on mica,^{20, 21} or randomly oriented on Si/SiO₂,⁴⁵ the NWs have a triangular cross-section with the same (110) planes parallel to the surface and the (100) and (010) planes forming the side walls of the triangular prism. This specific and recurring structure can be rationalized considering that the (100) facets are probably the most stable ones (although no surface energies have been calculated for the cubic phase, the (100) was calculated to be the most stable one for the tetragonal phase).⁴⁷ This could also explain, to some

extent, the differences between the structure and form of NWs that grow in vapor phase compared to solution-grown NWs, where often the surface energy is governed by surface ligands.⁴⁸

When combining these reports with this work, where the guided NWs exhibit the same structure on flat and faceted sapphire substrates (figure 2C), we can speculate that in the vapor-phase growth of CsPbBr₃ NWs, the anisotropic growth that leads to the 1D geometry and the crystallographic orientation of the NWs is independent of the substrate. If this is true, then the different substrates, with their specific properties and symmetries, affect only the growth directions of the NWs with respect to the substrate. It follows that surface-bound CsPbBr₃ NWs will grow randomly on an amorphous substrate, as in the case of a Si/SiO₂ substrate,⁴⁵ and for sapphire or mica substrates they will grow along certain directions that are imposed by the crystal (epitaxy) or the morphology (graphoepitaxy) of the substrate.^{20, 21}

A possible explanation for the apparent negligible effect that different substrates have on the crystallographic orientation of surface-bound CsPbBr₃ NWs, as opposed to guided NWs of more classical “hard” semiconductors, is the “soft” nature of lead halide perovskites. CsPbBr₃, and more commonly hybrid organic-inorganic lead halide perovskites, are often referred to as soft ionic crystals.⁴⁹⁻⁵¹ If we assume that the horizontal growth process is thermodynamically governed and that softer material can accommodate crystal frustration and stress with less energetic cost, we can hypothesize that in the case of CsPbBr₃ NWs, the energetic cost of accommodating to the surface is not high enough to justify a transition to a less energetically preferred crystallographic orientation. In this scenario, the NWs will grow to the energetically preferred crystallographic orientation regardless to the substrate they grow on. The substrate, however, does affect the growth direction of the NWs. The growth direction along nanogrooves in a graphoepitaxial growth is dictated by surface features, and for epitaxial growth on sapphire, the lattices of the perovskite and

sapphire seem to align nicely through the planes that are orthogonal to the interface along and across the growth axis of the NWs.

For optical characterization, room-temperature PL spectra were obtained using a micro-Raman system (Horiba LabRAM HR Evolution) with a 325 nm He-Cd laser. Under the optical microscope, visible green luminescence was apparent at the excitation spot, and also at both ends of the NWs, as can be seen in figure 3a. Since the reported lasing abilities of similar NWs depend on significant end-facet reflectivity and efficient wave guiding along their length,^{17, 52} it is reasonable to attribute the green emission at the ends of the NWs to the propagation of the PL emission along them as they serve as waveguides.

PL spectra were measured for many single guided CsPbBr₃ NWs, generally exhibiting a strong single peak around 520 nm with full width half maximum (FWHM) of about 15 nm. This is comparable to previous reports on CsPbBr₃ NWs and suggests a high crystal quality.^{17, 20, 21, 45, 52} We used the large spread in the diameters of the NWs (20-2000 nm) in order to explore possible size-dependent optical phenomena, and noticed that the emission peak for larger NWs is red shifted compared to the thinner ones. In order to quantify this observation, the heights of 10 NWs with different diameters were measured using tapping mode atomic force microscope (AFM) and their corresponding PL spectra were taken (figure 3b-c). It is noticeable that the emission peak red shifts with increasing height of the NWs. Surprisingly this size-dependent effect is in play for NWs with heights spanning from 45 nm to almost 1.5 μm , λ_{max} shifts from 514 nm to 528 nm respectively. Additional intensity-dependent measurements can be found in the Supporting Information (figure S6). This trend can be seen also along a single tapered NW (figure 3d). In this case, the height of the NW is constant from the top edge to half the length of the NW at ~125 nm (position 60-30 in figure 3d) and the corresponding PL emission peaks are constant as well at ~519 nm. Once the

NW starts to taper from 125 nm to 65 nm (position 30-0 in image 32d), the emission peak gradually shifts from ~519 nm to ~516 nm.

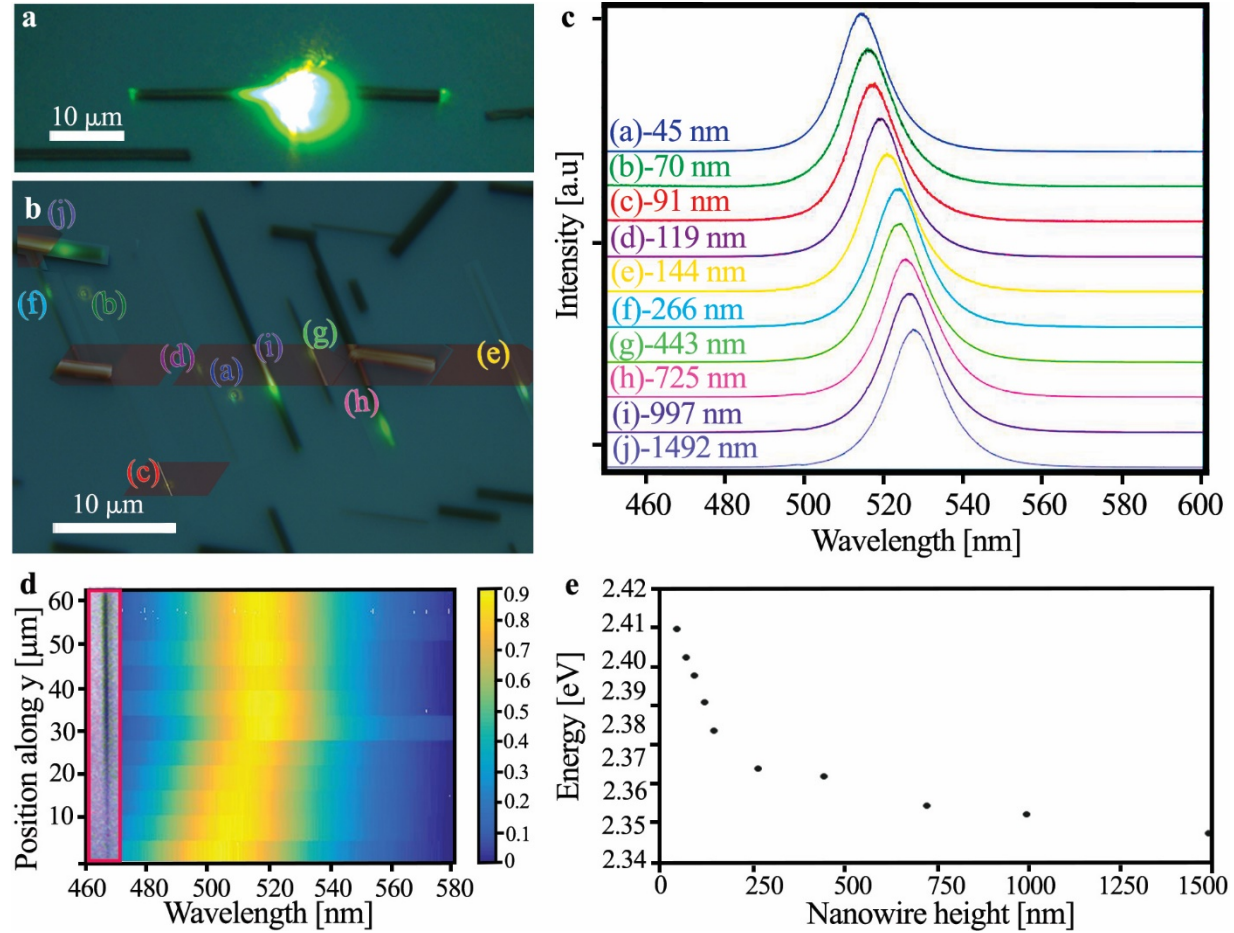


Figure 3. Optical properties of guided CsPbBr₃ NWs. (a) Optical microscope image of a guided CsPbBr₃ NW exhibiting green photoluminescence from the excitation spot and both ends of the NW. (b) Optical microscope image of NWs with different sizes overlaid by the AFM height images. Green spots are the locations of the room-temperature PL spectra measurements presented in (c) along with the measured height of the NWs. (d) Normalized intensity PL map along a tapered NW (seen in the red inset). (e) Optical band gap as a function of the measured height of 10 different NWs under 100 W/cm² illumination of a 325 nm UV laser.

When we tried to understand the origin of this relatively small, but consistent and meaningful size dependent phenomenon, five mechanisms (i-v) were taken into consideration. We shall start by ruling out the less likely mechanisms, and then focus on the more plausible ones. (i) Quantum confinement: Plotting the optical band gap versus the height of the NWs (figure 3e) discloses a trend that resembles previous reports on quantum confinement in NWs.^{53, 54} It is clear, however, that the dimensions of these guided CsPbBr₃ NWs are well beyond the quantum confinement regime, as the Bohr-exciton radius was calculated to be 7.5 nm.⁵⁵ Beyond the quantum confinement regime, energy shifts could be explained by surface depletion induced quantum confinement.⁵⁶ This additional mechanism can explain confinement in larger diameters than that of the Bohr-exciton diameter, but cannot explain red shifts in the micrometer regime as observed. Future temperature dependent measurements should provide a more decisive conclusion since the surface depletion induced quantum confinement diminishes with decreasing temperatures. (ii) Thermal effect: Another reason for energy shifts upon illumination is local heating and its effect on the crystal structure, and therefore the band gap of a semiconductor, known as the Varshni shift.⁵⁷ However for CsPbBr₃, and other perovskites as well, the optical band gap shifts to lower energies with decreasing temperature due to a positive thermal expansion coefficient.^{58, 59} If we consider that local heating increases with size,⁶⁰ we would expect larger NWs to be subjected to more local heating that would lead to higher band gap energies. This translate to a blue shift with increasing NW-size, which is opposite to our observations. (iii) Surface field-effect and photon reabsorption: Double charged surface layers in lead halide perovskite crystal was also suggested to induce an increase of the optical bandgap compared to the bulk due to a macroscopic electric field that is generated near the surface of thin films owing to spontaneous separation of halide ions and positively charged vacancies.⁶¹ Although surface phenomena are always considered possible

origins to bulk-nanostructure discrepancies, the double charge surface layer hypothesis is based on reabsorption of high energy photons in a surface layer which is on the order of 1 μm , while our NWs are typically much smaller. This reduces the validity of this phenomenon as an explanation to the size-dependent energy shift we observe. With that said, excitation and emission spectra studies are underway in order to confirm or refute this hypothesis, and other processes that involve reabsorption, such as photon recycling.⁸

Although we are still not able to determine unambiguously the origin of the emission red shift with increasing NW diameter beyond the quantum confinement regime, we consider two more possible effects. One is strain-induced band gap modulation and the other is the band filling effect also known as the Burstein-Moss (BM) effect.⁶² (iv) Strain: Anomalous phenomena are not rare among lead halide perovskites, and most of them trace back to the unique crystal structure of these materials.¹⁰ The relationship between the structure and the optical bandgap of lead-halide perovskite, and more specifically, change in the Pb-I bond stress in the case of methylammonium lead iodide, was suggested as the origin of an absorption and emission red shifts in thin films composed of large crystallites compared to films composed of smaller crystallites.^{63, 64} This claim was based on several studies exploring the effect of the structure, bond lengths and angles, on the optical bandgap of lead-halide perovskites.^{65, 66} A recent first-principles study also found that external pressure can result in a bandgap red shift in CsPbBr_3 due to changes in the Pb-Br bond length and angle.⁶³ Therefore, the observed red shift could also be explained by a change in the Pb-Br stress as in the case of larger crystallites in methylammonium lead iodide films.^{63, 64} Moreover, as discussed earlier, the selected area FFTs of our NWs imply the existence of either phase domain boundaries or Ruddlesden–Popper domains within the guided CsPbBr_3 NWs. The accumulated strain induced by these domains, by exposing certain facets to the environment and

by substrate interactions could cause enhanced structural deformation that might cause a more noticeable modulation of the band gap. We expect the NWs with larger diameters to be more strained,⁶⁷ leading to a red shift that matches, at least qualitatively, our observation.⁶⁸ (v) The band filling effect, also known as the Burstein-Moss (BM) effect provides another possible explanation for our observations, and is often used to explain otherwise unexplained blue shifts in nanostructures as their size decrease.⁶⁹ Further work must be done in order to determine the exact origin of this phenomenon. Geometric phase analysis (GPA) can perhaps be used to quantify the strain in NWs with different dimensions to verify or refute the strain related approach. Further PL measurements combined with an appropriate model could be used to estimate the role that the BM effect plays in the size dependent emission shift we observe.

We note that if this is a strain-induced emission shift, it could be in play also in vertical NWs, however the magnitude of the strain, and thus the observed shifts might be substantially larger for surface bound perovskite NWs due to their interaction with the substrate. A strain-dependent phenomenon that is well established, quantified and calibrated could be used to assess strain in other CsPbBr₃ system as well. Regardless to the origin of this phenomenon, we demonstrate that the optical band gap of guided inorganic halide perovskite NWs can be fine-tuned through their size. Small shifts in the optical band gap of these structures could be useful for future optoelectronic applications.

Recently, high-performance photodetectors based on thin films and nanostructure networks of CsPbBr₃ were reported.^{21, 30-37} However, to the best of our knowledge, the electronic and optoelectronic behavior of a single NW or small arrays of CsPbBr₃ guided NWs was not yet reported, and is essential to better understand this system and to determine the potential of guided CsPbBr₃ NWs as building blocks for optoelectronic applications. Previous studies conducted on

surface-guided NWs show that despite the substrate-NW interactions they exhibit very good optoelectronic properties. In fact, photodetectors based on guided NWs of ZnSe,²³ CdSe,²⁵ and CdS²⁸ outperformed their vertical counterparts. It is therefore interesting to assess the optoelectronic properties of our CsPbBr₃ NWs and compare them with other devices.

In order to probe the electronic and optoelectronic properties of guided CsPbBr₃ NWs we exploited the deterministic control over their growth direction and fabricated multiple devices using only a single fabrication step. We used a custom made shadow mask (Suron) with a 10 μ m channel and used electron-beam deposition to fabricate C/Ti electrodes (10 nm/100 nm). Since the NWs nucleate randomly on the substrate, statistically the number of NWs that cross the channel between the electrodes was determined by the density of the guided NWs, their length and the channel location imposed by the shadow mask. Alternatively, electron-beam lithography can be used for better control over the dimensions and location of the contacts.¹⁸ A typical photodetector has between 1 to 10 CsPbBr₃ guided NWs with relatively large diameters that cross a 10-20 μ m gap between the electrodes (figure S7).

On the basis of the described devices, FETs were also fabricated using atomic layer deposition (ALD) to deposit a 50 nm dielectric layer of Al₂O₃, followed by fabrication of Cr/Au (5/50 nm) gate electrode using standard photolithography and e-beam evaporation. Once the devices were fabricated, we used a Janis ST-500 probe system with a Keithley 4200-SCS to conduct *I-V* measurements under different gate voltages. We find that the devices are gate-responsive and that they qualitatively exhibit a p-type behavior (Figure S8). However, after the ALD deposition we observed substantial hysteresis and temporal changes in the source-drain current under constant biases with some devices. In order to assess the behavior of such FETs in a quantitative manner, we must acquire a deeper understanding of the hysteresis phenomenon. We plan to study these

behaviors using different fabrication processes and materials for the gate dielectric, and by conducting the gate dependent measurements under cryogenic conditions. We aim to reach conditions where the hysteresis is negligible so we can extract the correct mobilities and charge carrier concentrations of the guided CsPbBr₃ NWs.

For optoelectronic measurements, we used the Janis ST-500 probe system with a Keithley 4200-SCS coupled to an optical table and a 473 nm power-tunable laser. *I-V* measurements were done under vacuum, at room temperature, in dark condition ($\sim 20 \mu\text{W}/\text{cm}^2$ ambient light) and under different illumination intensities of the 473 nm laser. Measurements were conducted on photodetectors based on guided CsPbBr₃ NWs that grew on C-plane and annealed M-plane sapphire. Typical devices can be seen in figure 4A-B respectively. For the photodetectors on each plane; *I-V* curves were measured at different illumination intensities and on-off switching cycles were also measured in order to characterize the response times.

The photodetectors fabricated on C-plane show low dark currents of $\sim 15 \text{ pA}$ under a 1 V bias. Illumination of $220 \text{ mW}/\text{cm}^2$ under the same bias results in a current increase of more than 3 orders of magnitude to $\sim 50 \text{ nA}$. We note that the *I-V* curves on this device appear to reach current saturation around $\pm 1 \text{ V}$ under illumination. We do not observe the same current saturation behavior with the photodetectors fabricated on annealed M-plane. Although the *I-V* curves for the annealed M-plane photodetectors show a slightly different behavior than the C-plane photodetector, with respect to the current saturation, they are also photoresponsive, and under 1 V bias they exhibit a dark current of $\sim 15 \text{ pA}$ and more than 3 orders of magnitude increase to $\sim 75 \text{ nA}$ upon illumination of $115 \text{ mW}/\text{cm}^2$.

The photoresponse speed is an important parameter in a photodetector characteristics. The rise time is defined as the time required for the photocurrent to increase from 10% to 90%, and the fall

time is defined *vice versa*. Rise and decay time constants devices can be determined by fitting to exponential curves: $I_{\text{photo}} = I_{\text{photo},0}[1 - \exp(-t/\tau_r)]$ for the rise and $I_{\text{photo}} = I_{\text{photo},0}[\exp(-t/\tau_d)]$ for the fall. Where $I_{\text{photo},0}$ is the maximum photocurrent, t is the time, τ_r and τ_d are the rise and decay time constants respectively. In order to measure the expected fast response of the photodetectors we used an acousto-optic modulator (AOM) to shift the laser beam on and off the device, achieving fast laser reaction (< 200 ns). The light switching frequency was controlled with a function generator. The devices were exposed to various frequencies of on/off cycles under a 10 V bias. On/off cycles were measured for the photodetector fabricated on C-plane under illumination of 113 mW/cm^2 , revealing rise and fall times of $71 \text{ }\mu\text{s}$ and $68 \text{ }\mu\text{s}$ respectively with corresponding time constants of $\tau_r=31 \text{ }\mu\text{s}$ and $\tau_d=30 \text{ }\mu\text{s}$. Similar measurements on the photodetector fabricated on annealed M-plane under illumination of 100 mW/cm^2 , revealed rise and fall times of $10.4 \text{ }\mu\text{s}$ and $5.3 \text{ }\mu\text{s}$ respectively with time constants of $\tau_r=5.2 \text{ }\mu\text{s}$ and $\tau_d=3.2 \text{ }\mu\text{s}$. All the devices show high repeatability and stable results during the measurements.

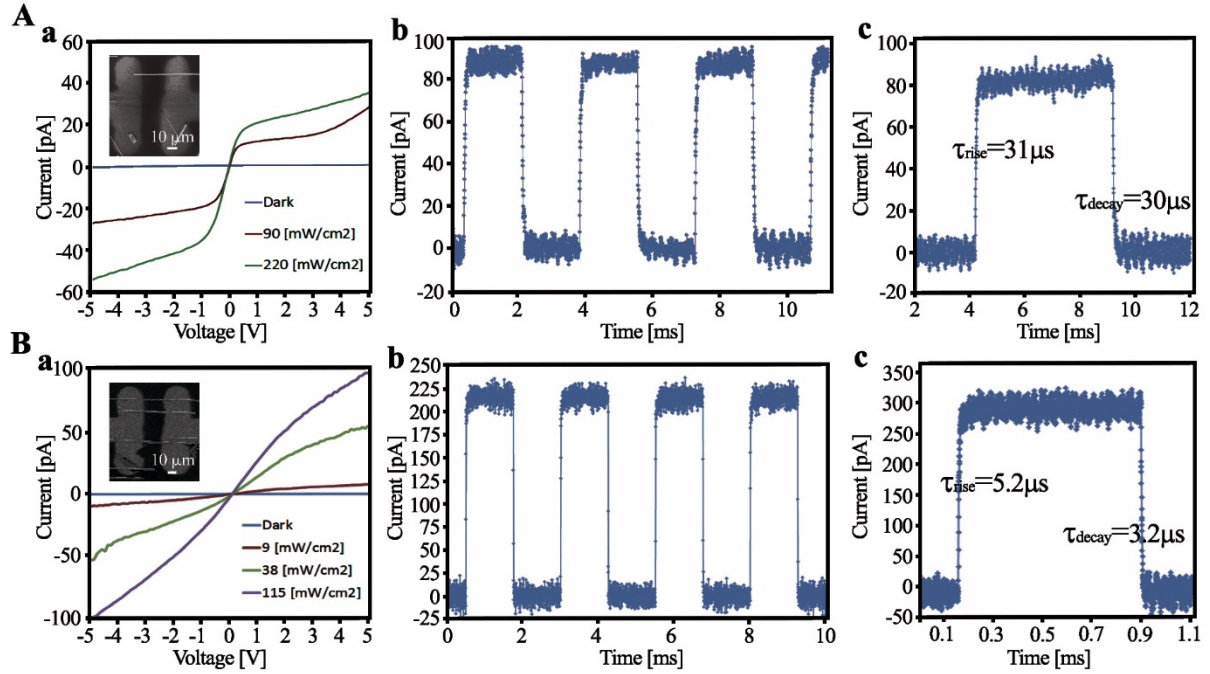


Figure 4. Performance of photodetectors based on guided CsPbBr₃ NWs fabricated on C-plane (A) and annealed M-plane (B) sapphire. For the photodetectors on each plane (a) *I-V* curves at different illumination intensities and a SEM image of a typical device in the inset. (b) Few cycles and a (c) single cycle of on-off switching (under 10 V bias and 100-113 mW/cm² illumination of a 473 nm laser for C-plane and annealed M-plane respectively) with their calculated rise and decay time constants.

These results highlight differences between the photodetectors fabricated on C-plane and on annealed M-plane. Their *I-V* curves show somewhat different trends and the rise and decay time constants of the C-plane photodetectors are an order of magnitude slower than those of the photodetector fabricated on annealed M-plane. At this point we cannot offer a well-supported and reliable explanation for these differences, in part because our devices are usually based on small arrays of NWs with different diameters. The diameter of the CsPbBr₃ NWs could affect their properties and the performance of devices based on them. Therefore, in order to correlate between

the different substrates and the performances of devices fabricated on them, future work will focus on measurements of equivalent and well characterized single-NW devices on different sapphire planes using a controlled electron-beam fabrication. Since, to the best of our knowledge, these are the first electrical transport measurements performed on a single NW or small arrays of planar CsPbBr₃ NWs, we cannot compare our results with other reports. However when comparing these results to thin films, large single crystals and other nanostructure-networks (table 1), we find that the 3 orders of magnitude on/off ratio is comparable to most reports and that our response times are faster than any CsPbBr₃ based photodetector.^{21, 30-37} We attribute the fast response times of our photodetectors mainly to the high quality, single crystal nature of our NWs and to the fact that in most other reports the nanostructures are arranged in networks or films with multiple grains and grain boundaries.

Table 1. Photodetectors based on CsPbBr₃.

Photodetectors based on	On off ratio (order of magnitude)	Rise time	Decay Time	Ref.
Few horizontal NW-arrays	10 ³	10 μ s	5 μ s	Our work
Horizontal NW-networks	10 ³	<0.1 s	<0.1 s	21
Fused films	10 ³	0.35 ms	1.26 ms	30
Films	10 ³	30 ms	114 ms	31
Thin films	10 ⁵	430 μ s	318 μ s	32
Bulk single crystal	10 ²	<100 ms	<100 ms	33
Bulk single crystal	10 ⁵	230 ms	30 ms	34
Monolayer and few-layer nanostructures	10 ³	19 μ s	25 μ s	35
Colloidal nanosheets	10 ²	17 ms	15 ms	36
Nanocrystals layer	10 ⁵	24 ms	29 ms	37
Single-crystal thin films	-	Several milliseconds		38

To conclude, we have demonstrate guided growth of horizontally aligned CsPbBr₃ NWs on flat and faceted sapphire substrates. We characterize the crystal structure of NWs that grow epitaxially in a 6-fold symmetry on flat C-plane sapphire and NWs that grow along nanogrooves in a bidirectional growth leading to parallel arrays, which are well suited for application and research. We find that that all the CsPbBr₃ guided NWs have an isosceles right triangular cross-section and grow along the same [001] crystallographic orientation of the CsPbBr₃ cubic phase. Using a relatively large spread in the diameters of the NWs (20-2000 nm), we find a size dependent PL emission shift well beyond the quantum regime as the emission peak red shifts with increasing diameter from 514 nm to 528 nm for NWs with diameters of 45 nm and 1.5 μ m respectively. We

exploit the controlled directional growth of the guided NWs to demonstrate the fabrication and measurements of devices based on a single NW or parallel arrays of few CsPbBr₃ guided NWs that are all in contact with the electrodes. Only a single evaporation step through a costume-made shadow mask is needed to form electrodes and create multiple photodetectors and probe the intrinsic properties of CsPbBr₃ nanostructures that are not arrange in networks or films in which the behavior is often governed by multiple grains boundaries. The photodetectors based on guided CsPbBr₃ NWs exhibit faster response times than any CsPbBr₃ based photodetector reported so far. A p-type electronic behavior was also determined through field-effect measurements. This epitaxial and graphoepitaxial growth of horizontal arrays of CsPbBr₃ guided NWs with promising properties that are easily integrated into devices demonstrates the great potential of guided NWs of lead halide perovskites for future research and applications.

ASSOCIATED CONTENT

Supporting Information: (1) Methods and synthesis scheme. (2) HRTEM of guided CsPbBr₃ on C-plane sapphire. (3) Powder XRD measurements. (4) Nanowires grow along different numbers of nanogrooves along their growth axis. (5) Half unit cell peaks in selected area FFT (6) Intensity-dependent PL measurements (7) Optical images of photodetectors base on guided CsPbBr₃ NWs. (8) FETs based on guided CsPbBr₃ NWs.

AUTHOR INFORMATION

Corresponding Author

**E-mail: ernesto.joselevich@weizmann.ac.il

Funding Sources

European Research Council (ERC) Advanced Grant (No. 338849).

Notes

The authors declare no competing financial interest.

ACKNOWLEDGMENT

We thank David Cahen, Gary Hodes, Omer Yaffe, Regev Ben-Zvi, Michael Kulback and Yevgeny Rakita for helpful discussions. We thank Yishay (Isai) Feldman for conducting the powder XRD measurements. This research was supported by the European Research Council (ERC) Advanced Grant (No. 338849), Helena and Martin Kimmel Center for Nanoscale Science, Moskowitz Center for Nano and Bio-Nano Imaging, and the Carolito Stiftung. E.J. holds the Drake Family Professorial Chair of Nanotechnology.

ABBREVIATIONS

VLS, vapor-liquid-solid; FIB, focused ion beam; HRTEM, high resolution transmission electron microscope; SEM, scanning electron microscope; AFM, atomic force microscope; PL, photoluminescence; EMCCD, electron multiplying charge-coupled device; TEM, transmission electron microscope; EDS, Energy-dispersive X-ray spectroscopy; FET, field effect transistor; STEM, scanning transmission electron microscopy; GPA, geometric phase analysis.

REFERENCES

1. Zhang, W.; Eperon, G. E.; Snaith, H. J. **2016**, 1, 16048.
2. Kojima, A.; Teshima, K.; Shirai, Y.; Miyasaka, T. *J. Am. Chem. Soc.* **2009**, 131, (17), 6050-6051.
3. Yang, W. S.; Noh, J. H.; Jeon, N. J.; Kim, Y. C.; Ryu, S.; Seo, J.; Seok, S. I. *Science* **2015**, 348, (6240), 1234-1237.
4. Stranks, S. D.; Snaith, H. J. *Nat. Nanotechnol.* **2015**, 10, (5), 391-402.

5. Zhu, H.; Fu, Y.; Meng, F.; Wu, X.; Gong, Z.; Ding, Q.; Gustafsson, M. V.; Trinh, M. T.; Jin, S.; Zhu, X. Y. *Nat. Mater.* **2015**, 14, (6), 636-642.
6. Deng, W.; Huang, L.; Xu, X.; Zhang, X.; Jin, X.; Lee, S.-T.; Jie, J. *Nano Lett.* **2017**, 17, (4), 2482-2489.
7. Stranks, S. D.; Eperon, G. E.; Grancini, G.; Menelaou, C.; Alcocer, M. J. P.; Leijtens, T.; Herz, L. M.; Petrozza, A.; Snaith, H. J. *Science* **2013**, 342, (6156), 341-344.
8. Pazos-Outón, L. M.; Szumilo, M.; Lamboll, R.; Richter, J. M.; Crespo-Quesada, M.; Abdi-Jalebi, M.; Beeson, H. J.; Vrućinić, M.; Alsari, M.; Snaith, H. J.; Ehrler, B.; Friend, R. H.; Deschler, F. *Science* **2016**, 351, (6280), 1430-1433.
9. Leijtens, T.; Stranks, S. D.; Eperon, G. E.; Lindblad, R.; Johansson, E. M. J.; McPherson, I. J.; Rensmo, H.; Ball, J. M.; Lee, M. M.; Snaith, H. J. *ACS Nano* **2014**, 8, (7), 7147-7155.
10. Brenner, T. M.; Egger, D. A.; Kronik, L.; Hodes, G.; Cahen, D. **2016**, 1, 15007.
11. Snaith, H. J.; Abate, A.; Ball, J. M.; Eperon, G. E.; Leijtens, T.; Noel, N. K.; Stranks, S. D.; Wang, J. T.-W.; Wojciechowski, K.; Zhang, W. *J. Phys. Chem. Lett.* **2014**, 5, (9), 1511-1515.
12. Frost, J. M.; Walsh, A. *Acc. Chem. Res.* **2016**, 49, (3), 528-535.
13. La-o-vorakiat, C.; Salim, T.; Kadro, J.; Khuc, M. T.; Haselsberger, R.; Cheng, L.; Xia, H. X.; Gurzadyan, G. G.; Su, H. B.; Lam, Y. M.; Marcus, R. A.; Michel-Beyerle, M. E.; Chia, E. E. M. *Nat. Commun.* **2016**, 7.
14. Saliba, M.; Matsui, T.; Seo, J.-Y.; Domanski, K.; Correa-Baena, J.-P.; Nazeeruddin, M. K.; Zakeeruddin, S. M.; Tress, W.; Abate, A.; Hagfeldt, A.; Gratzel, M. *Energy Environ Sci.* **2016**, 9, (6), 1989-1997.
15. Kulbak, M.; Gupta, S.; Kedem, N.; Levine, I.; Bendikov, T.; Hodes, G.; Cahen, D. *J. Phys. Chem. Lett.* **2016**, 7, (1), 167-172.
16. Kulbak, M.; Cahen, D.; Hodes, G. *J. Phys. Chem. Lett.* **2015**, 6, (13), 2452-2456.
17. Eaton, S. W.; Lai, M.; Gibson, N. A.; Wong, A. B.; Dou, L.; Ma, J.; Wang, L.-W.; Leone, S. R.; Yang, P. *Proc. Natl. Acad. Sci.* **2016**, 113, (8), 1993-1998.
18. Dou, L.; Lai, M.; Kley, C. S.; Yang, Y.; Bischak, C. G.; Zhang, D.; Eaton, S. W.; Ginsberg, N. S.; Yang, P. *Proc. Natl. Acad. Sci.* **2017**, 114, (28), 7216-7221.
19. Fu, Y.; Zhu, H.; Stoumpos, C. C.; Ding, Q.; Wang, J.; Kanatzidis, M. G.; Zhu, X.; Jin, S. *ACS Nano* **2016**, 10, (8), 7963-7972.
20. Wang, Y.; Sun, X.; Shivanna, R.; Yang, Y.; Chen, Z.; Guo, Y.; Wang, G.-C.; Wertz, E.; Deschler, F.; Cai, Z.; Zhou, H.; Lu, T.-M.; Shi, J. *Nano Lett.* **2016**, 16, (12), 7974-7981.
21. Chen, J.; Fu, Y.; Samad, L.; Dang, L.; Zhao, Y.; Shen, S.; Guo, L.; Jin, S. *Nano Lett.* **2017**, 17, (1), 460-466.
22. Oksenberg, E.; Martí-Sánchez, S.; Popovitz-Biro, R.; Arbiol, J.; Joselevich, E. *ACS Nano* **2017**, 11, (6), 6155-6166.
23. Oksenberg, E.; Popovitz-Biro, R.; Rechav, K.; Joselevich, E. *Adv. Mater.* **2015**, 27, (27), 3999-4005.
24. Reut, G.; Oksenberg, E.; Popovitz-Biro, R.; Rechav, K.; Joselevich, E. *J. Phys. Chem. C* **2016**, 120, (30), 17087-17100.
25. Shalev, E.; Oksenberg, E.; Rechav, K.; Popovitz-Biro, R.; Joselevich, E. *ACS Nano* **2017**, 11, (1), 213-220.
26. Tsivion, D.; Schwartzman, M.; Popovitz-Biro, R.; Joselevich, E. *ACS Nano* **2012**, 6, (7), 6433-6445.
27. Tsivion, D.; Schwartzman, M.; Popovitz-Biro, R.; von Huth, P.; Joselevich, E. *Science* **2011**, 333, (6045), 1003-1007.

28. Xu, J.; Oksenberg, E.; Popovitz-Biro, R.; Rechav, K.; Joselevich, E. *J. Am. Chem. Soc.* **2017**.
29. Tsivion, D.; Joselevich, E. *Nano Lett.* **2013**, 13, (11), 5491-5496.
30. Xue, J.; Gu, Y.; Shan, Q.; Zou, Y.; Song, J.; Xu, L.; Dong, Y.; Li, J.; Zeng, H. *Angew. Chem., Int. Ed.* **2017**, 56, (19), 5232-5236.
31. Li, X.; Yu, D.; Cao, F.; Gu, Y.; Wei, Y.; Wu, Y.; Song, J.; Zeng, H. *Adv. Funct. Mater.* **2016**, 26, (32), 5903-5912.
32. Li, Y.; Shi, Z.-F.; Li, S.; Lei, L.-Z.; Ji, H.-F.; Wu, D.; Xu, T.-T.; Tian, Y.-T.; Li, X.-J. *J. Mater. Chem. C* **2017**.
33. Ding, J.; Du, S.; Zuo, Z.; Zhao, Y.; Cui, H.; Zhan, X. *J. Phys. Chem. C* **2017**, 121, (9), 4917-4923.
34. Saidaminov, M. I.; Haque, M. A.; Almutlaq, J.; Sarmah, S.; Miao, X.-H.; Begum, R.; Zhumeckenov, A. A.; Dursun, I.; Cho, N.; Murali, B.; Mohammed, O. F.; Wu, T.; Bakr, O. M. *Adv. Opt. Mater.* **2017**, 5, (2), 1600704-n/a.
35. Song, J.; Xu, L.; Li, J.; Xue, J.; Dong, Y.; Li, X.; Zeng, H. *Adv. Mater.* **2016**, 28, (24), 4861-4869.
36. Lv, L.; Xu, Y.; Fang, H.; Luo, W.; Xu, F.; Liu, L.; Wang, B.; Zhang, X.; Yang, D.; Hu, W.; Dong, A. *Nanoscale* **2016**, 8, (28), 13589-13596.
37. Ramasamy, P.; Lim, D.-H.; Kim, B.; Lee, S.-H.; Lee, M.-S.; Lee, J.-S. *Chem. Commun.* **2016**, 52, (10), 2067-2070.
38. Chen, J.; Morrow, D. J.; Fu, Y.; Zheng, W.; Zhao, Y.; Dang, L.; Stolt, M. J.; Kohler, D. D.; Wang, X.; Czech, K. J.; Hautzinger, M. P.; Shen, S.; Guo, L.; Pan, A.; Wright, J. C.; Jin, S. *J. Am. Chem. Soc.* **2017**, 139, (38), 13525-13532.
39. Nikoobakht, B.; Herzing, A. *Nanoscale* **2014**, 6, (21), 12814-12821.
40. Gabai, R.; Ismach, A.; Joselevich, E. *Adv. Mater.* **2007**, 19, (10), 1325-1330.
41. Zhang, D.; Eaton, S. W.; Yu, Y.; Dou, L.; Yang, P. *J. Am. Chem. Soc.* **2015**, 137, (29), 9230-9233.
42. Yu, Y.; Zhang, D.; Yang, P. *Nano Lett.* **2017**.
43. Yu, Y.; Zhang, D.; Kisielowski, C.; Dou, L.; Kornienko, N.; Bekenstein, Y.; Wong, A. B.; Alivisatos, A. P.; Yang, P. *Nano Lett.* **2016**, 16, (12), 7530-7535.
44. Dang, Z.; Shamsi, J.; Palazon, F.; Imran, M.; Akkerman, Q. A.; Park, S.; Bertoni, G.; Prato, M.; Brescia, R.; Manna, L. *ACS Nano* **2017**, 11, (2), 2124-2132.
45. Zhou, H.; Yuan, S.; Wang, X.; Xu, T.; Wang, X.; Li, H.; Zheng, W.; Fan, P.; Li, Y.; Sun, L.; Pan, A. *ACS Nano* **2017**, 11, (2), 1189-1195.
46. Wang, X.; Zhou, H.; Yuan, S.; Zheng, W.; Jiang, Y.; Zhuang, X.; Liu, H.; Zhang, Q.; Zhu, X.; Wang, X.; Pan, A. *Nano Res* **2017**.
47. Niu, G.; Yu, H.; Li, J.; Wang, D.; Wang, L. *Nano Energy* **2016**, 27, (Supplement C), 87-94.
48. Boles, M. A.; Ling, D.; Hyeon, T.; Talapin, D. V. *Nat. Mater.* **2016**, 15, 141.
49. Rakita, Y.; Cohen, S. R.; Kedem, N. K.; Hodes, G.; Cahen, D. *MRS Commun.* **2015**, 5, (4), 623-629.
50. Tsutomu, M. *Chem. Lett.* **2015**, 44, (6), 720-729.
51. Yaffe, O.; Guo, Y.; Tan, L. Z.; Egger, D. A.; Hull, T.; Stoumpos, C. C.; Zheng, F.; Heinz, T. F.; Kronik, L.; Kanatzidis, M. G.; Owen, J. S.; Rappe, A. M.; Pimenta, M. A.; Brus, L. E. *Phys. Rev. Lett.* **2017**, 118, (13), 136001.
52. Park, K.; Lee, J. W.; Kim, J. D.; Han, N. S.; Jang, D. M.; Jeong, S.; Park, J.; Song, J. K. *J. Phys. Chem. Lett.* **2016**, 7, (18), 3703-3710.
53. Gudixsen, M. S.; Wang, J.; Lieber, C. M. *J. Phys. Chem. B* **2002**, 106, (16), 4036-4039.

54. Zhao, X.; Wei, C. M.; Yang, L.; Chou, M. Y. *Phys. Rev. Lett.* **2004**, 92, (23), 236805.
55. Protesescu, L.; Yakunin, S.; Bodnarchuk, M. I.; Krieg, F.; Caputo, R.; Hendon, C. H.; Yang, R. X.; Walsh, A.; Kovalenko, M. V. *Nano Lett.* **2015**, 15, (6), 3692-3696.
56. Li, D.; Zhang, J.; Xiong, Q. *ACS Nano* **2012**, 6, (6), 5283-5290.
57. Varshni, Y. P. *Physica* **1967**, 34, (1), 149-154.
58. D’Innocenzo, V.; Grancini, G.; Alcocer, M. J. P.; Kandada, A. R. S.; Stranks, S. D.; Lee, M. M.; Lanzani, G.; Snaith, H. J.; Petrozza, A. *Nat. Commun.* **2014**, 5, 3586.
59. Li, J.; Yuan, X.; Jing, P.; Li, J.; Wei, M.; Hua, J.; Zhao, J.; Tian, L. *RSC Adv.* **2016**, 6, (82), 78311-78316.
60. Han, L.; Zeman, M.; Smets, A. H. M. *Nanoscale* **2015**, 7, (18), 8389-8397.
61. Sarmah, S. P.; Burlakov, V. M.; Yengel, E.; Murali, B.; Alarousu, E.; El-Zohry, A. M.; Yang, C.; Alias, M. S.; Zhumekenov, A. A.; Saidaminov, M. I.; Cho, N.; Wehbe, N.; Mitra, S.; Ajia, I.; Dey, S.; Mansour, A. E.; Abdelsamie, M.; Amassian, A.; Roqan, I. S.; Ooi, B. S.; Goriely, A.; Bakr, O. M.; Mohammed, O. F. *Nano Lett.* **2017**, 17, (3), 2021-2027.
62. Prabhat, V.; Irmer, G.; Monecke, J. *J. Phys.: Condens. Matter* **2000**, 12, (6), 1097.
63. Xiao, G.; Cao, Y.; Qi, G.; Wang, L.; Liu, C.; Ma, Z.; Yang, X.; Sui, Y.; Zheng, W.; Zou, B. *J. Am. Chem. Soc.* **2017**, 139, (29), 10087-10094.
64. Fu, Y.; Meng, F.; Rowley, M. B.; Thompson, B. J.; Shearer, M. J.; Ma, D.; Hamers, R. J.; Wright, J. C.; Jin, S. *J. Am. Chem. Soc.* **2015**, 137, (17), 5810-5818.
65. Filip, M. R.; Eperon, G. E.; Snaith, H. J.; Giustino, F. *Nat. Commun.* **2014**, 5, 5757.
66. Amat, A.; Mosconi, E.; Ronca, E.; Quarti, C.; Umari, P.; Nazeeruddin, M. K.; Grätzel, M.; De Angelis, F. *Nano Lett.* **2014**, 14, (6), 3608-3616.
67. Wei, B.; Zheng, K.; Ji, Y.; Zhang, Y.; Zhang, Z.; Han, X. *Nano Lett.* **2012**, 12, (9), 4595-4599.
68. Grote, C.; Berger, R. F. *J. Phys. Chem. C* **2015**, 119, (40), 22832-22837.
69. Yang, Y. H.; Chen, X. Y.; Feng, Y.; Yang, G. W. *Nano Lett.* **2007**, 7, (12), 3879-3883.